

## Supplementary Materials for

### **Microfluidic device for the formation of optically excitable, three-dimensional, compartmentalized motor units**

Sebastien G. M. Uzel, Randall J. Platt, Vidya Subramanian, Taylor M. Pearl, Christopher J. Rowlands, Vincent Chan, Laurie A. Boyer, Peter T. C. So, Roger D. Kamm

Published 3 August 2016, *Sci. Adv.* **2**, e1501429 (2016)  
DOI: 10.1126/sciadv.1501429

#### **The PDF file includes:**

- Supplementary Materials and Methods
- fig. S1. DNA construct design, ESC colony morphology, DNA integration validation, and pluripotency characterization.
- fig. S2. Electrophysiological characterization of the ChR-HBG3-MN.
- fig. S3. Optogenetic activation of NMJs in adherent cocultures.
- fig. S4. Modes of tissue ablation.
- fig. S5. Photosensitization of the C2C12 myoblasts.
- fig. S6. Influence of the hydrogel on the force measured by the pillar.
- fig. S7. Motor neurite outgrowth in the microfluidic device.
- fig. S8. Opposite gradients as a mean to provide cell-specific medium.
- Legends for movies S1 to S4

**Other Supplementary Material for this manuscript includes the following:**  
(available at [advances.sciencemag.org/cgi/content/full/2/8/e1501429/DC1](http://advances.sciencemag.org/cgi/content/full/2/8/e1501429/DC1))

- movie S1 (.avi format). Muscle contraction upon optical stimulation of ChR-HBG3-MN in adherent cultures.
- movie S2 (.avi format). ECM compaction and muscle bundle formation over the first 96 hours of the experiment.
- movie S3 (.wmv format). 3D neurite outgrowth in the gel region bridging the neurosphere and the muscle strip.
- movie S4 (.avi format). Muscle bundle contraction upon light stimulation of the ChR-HBG3-MN in the microfluidic device.

## **Supplementary Materials and Methods**

### **Glial feeder layer cultures**

CD1 Mouse cortical glial cultures were provided by Dr. L.B. Wood, Beth Israel Deaconess Medical Center. Cultures were received in minimum essential medium (Sigma) with 10% horse serum (Sigma), 0.3% Anhydrous Dextrose (Fisher), 1x antibiotic antimycotic solution (Sigma).

### **Post deflection characterization**

The measurement device was previously described (79). Briefly, copper wire (Remington Industries, Johnsbury, IL) at 40 AWG size (87  $\mu\text{m}$  diameter), was cut approximately 2 cm in length and mounted on a 3-axis translation stage assembled from one MT1 (X-axis) and two DT12 dovetail (Y- and Z- axes) series manual translators (Thorlabs, Newton, NJ). The copper probe was calibrated by hanging known wire weights against gravity on the probe tip. The measurements were used to generate a load vs. displacement curve, which was then fit using linear regression. The stiffness of the copper probe was determined to be  $0.155 \mu\text{N} \cdot \mu\text{m}^{-1}$ .

The posts were immersed in cell culture medium. The probe tip was gently positioned and in contact with the top-center of the posts. The probe tip was directed to translate at 10  $\mu\text{m}$  intervals with return from 0  $\mu\text{m}$  (origin) to 200  $\mu\text{m}$  (20% post deflection) in the X-axis using the linear translator. A laser-optical sensor (optoNCDT 1401-1, Micro-Epsilon Optronic, Ortenburg, Germany) was used to measure position and displacement of the probe base. Software from the manufacturer (ILD1401 Tool v2.09, Micro-Epsilon Optronic, Ortenburg, Germany) was used to measure and record output values. Image sequences of the probe tip's position and displacement

were captured on the microscope stage (IX81, Olympus, Center Valley, PA 18034) by video capture software (Debut Video Capture, NCH Software, Greenwood Village CO) from a live acquisition software feed (MetaMorph, Molecular Devices, Sunnyvale, CA) using a digital CCD camera (ORCA-R2C10600-10B, Hamamatsu Photonics, Bridgewater, NJ).

The deflection of the post using the copper probe of known stiffness was used to determine the post stiffness. The post stiffness was measured to be  $0.36 \pm 0.08 \mu\text{N}\cdot\mu\text{m}^{-1}$  ( $n = 14$ ), within the range of values reported in previous studies (43, 88). For such a bending stiffness, the Young's modulus determined as a fitting parameter to the analytical solutions and computational simulations was found to be 1.26 and 1.11 MPa respectively, consistent with the 1 MPa measurement reported in the literature for a 5:1 mixing ratio (89).

### **Muscle bundle ablation**

*Manual ablation:* After 2 days in the microfluidic device, the reversibly bonded top layer of the device was gently peeled off and the tissue strips reminiscent of the gel filling channels and connector channel were ablated with a gauge 26 needle under a stereomicroscope. Medium was gently aspirated around the 2 muscle strips and a PDMS annulus was positioned on top of the bottom membrane in order to form a large medium reservoir (Fig. 4).

*2P-ablation:* Beside imaging (90) or local photoactivation of light-sensitive channels (91, 92) or 3D resolved photodynamic therapy (93), two-photon excitation has been used to generate microtracks by collagen ablation (94). We used a similar principle to ablate muscle tissue. Two-photon ablation was performed on a custom-built ablation setup. The beam from an ultrafast

laser (Spectra Physics, Mai Tai HP) of a 750 nm wavelength was expanded by a factor of 2 using two lenses in a 4f configuration (Newport, KPX094AR.16 and KPX106AR.16), then through a half waveplate (Newport, 10RP02-46) and Glan Thompson polarizer (Newport, 10GT04AR.16) for power control, before passing through a shutter (Oriel, 76992). The beam was further expanded by a factor of 3 using a beam expander (Thorlabs, BE03M-B) so as to fill the back aperture of the microscope objective. The resulting beam was then coupled into the back (fluorescence) port of a microscope body (Zeiss, Axiovert 40 CFL), where it reflected off the dichroic mirror (Semrock, FF750-SDi02-25x36) and passed into a 20x 0.5 numerical aperture air immersion objective (Zeiss, 440340-9904-000). The sample was simultaneously illuminated using brightfield illumination in order to image the ablation process; a camera (Thorlabs, DCC1545M) was used to capture the image. The sample was mounted on an automated microscope stage (Prior Scientific, HK01SKOP) however the stage was controlled manually. In order to perform tissue ablation, the microscope was first calibrated using a sample consisting of polymer nanospheres on a glass coverslip, in order to determine the location of the beam focus. The sample was then placed on the microscope and brought into focus, and the ablation turned on using the shutter. The beam was manually rastered across the sample in order to fully cut the tissue at the desired location (fig. S4, A and B). Care was taken so as to avoid ablating the PDMS and destroying the sample.

This technique has the advantage of performing ablation non-invasively in a closed environment and should be considered as the best alternative when opening the device is not an option. It could also be automated to carry out computer-aided multiple ablations.

Both manual and 2P technique yielded comparable results in terms of tissue tail resorption (fig. S4C), and muscle differentiation.

## Supplementary Figures

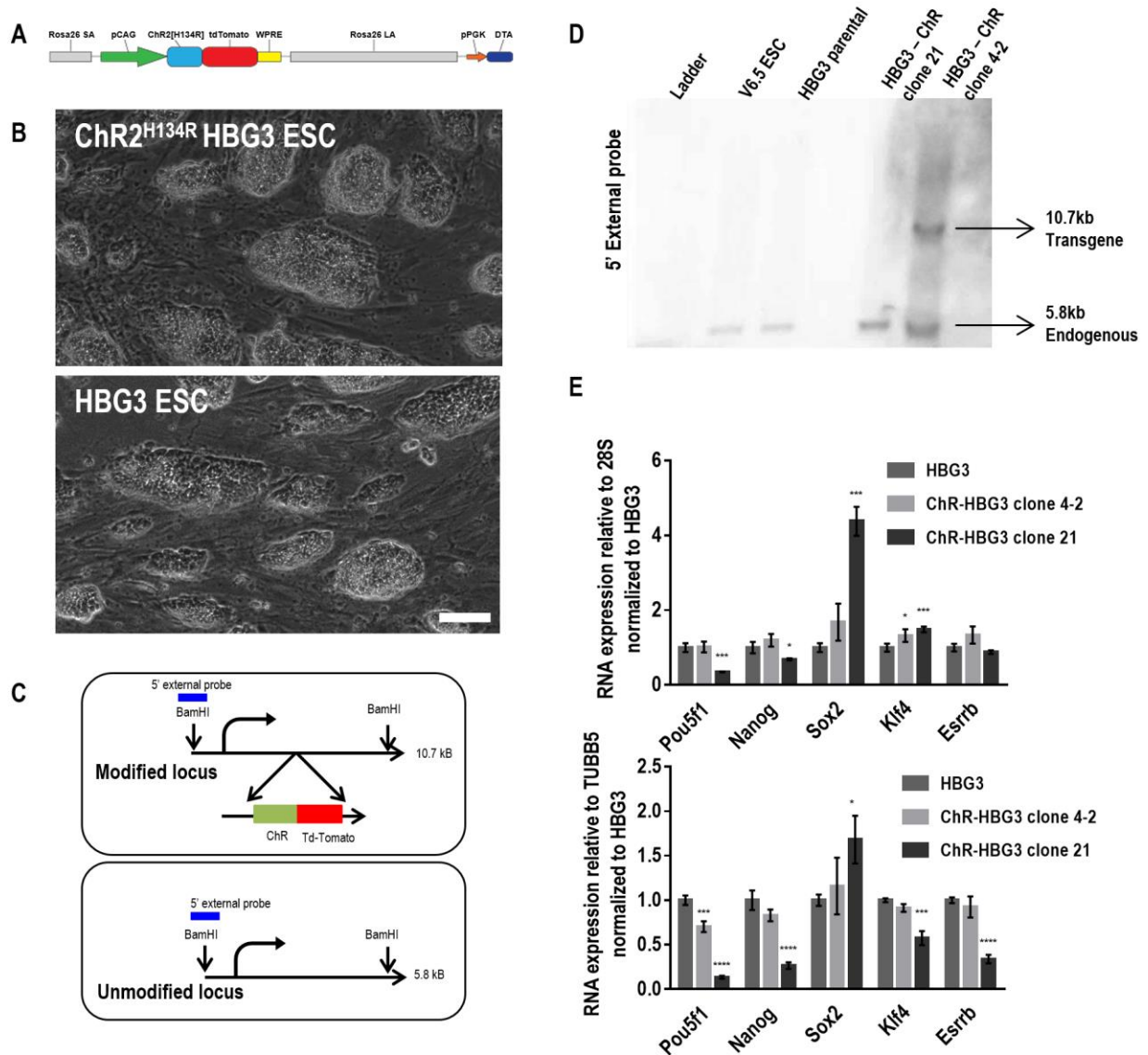


**fig. S1. Homologous recombination template design, integration validation and pluripotency characterization.** (A) Design of the DNA construct used for homologous recombination to generate cells containing Channelrhodopsin tdTomato (ChR) at the Rosa26 locus. (B) Comparison of the morphology of stem cell colonies between HBG3- and ChR-

HGB3-ESC. Scale bar: 100  $\mu$ m. **(C)** Schematic illustrating the southern blot strategy used to identify the clones that are rightly targeted at the Rosa26 locus. **(D)** Southern blots using radiolabeled probes against the Rosa26 promoter demonstrates the presence of a 10.8kb band in clone HGB3-ChR clone 4-2 suggesting the correct targeting of ChR at one of the Rosa26 allele (5.8kb band corresponds to the unmodified Rosa26 allele, seen in the wild type cells labeled-HGB3 parental). Contrastingly, the lack of this band in clone HGB3-Chr-21 suggests that targeting of the ChR gene did not occur at the Rosa26 locus. **(E)** Relative gene expression analyses using reverse transcription quantitative PCR for five pluripotency markers (Pou5f1, Nanog, Sox2, Kl4 and Esrrb) in the unmodified and recombined HGB3 cell lines. Unlike found in clone 21, the presence of the transgene in clone 4-2 has a minimal effect on the levels of expression of these markers. \*  $p < 0.05$ , \*\*  $p < 0.005$ , \*\*\*  $p < 0.0005$ , \*\*\*\*  $p < 0.0001$  (analysis of variance with respect to the control HGB3).

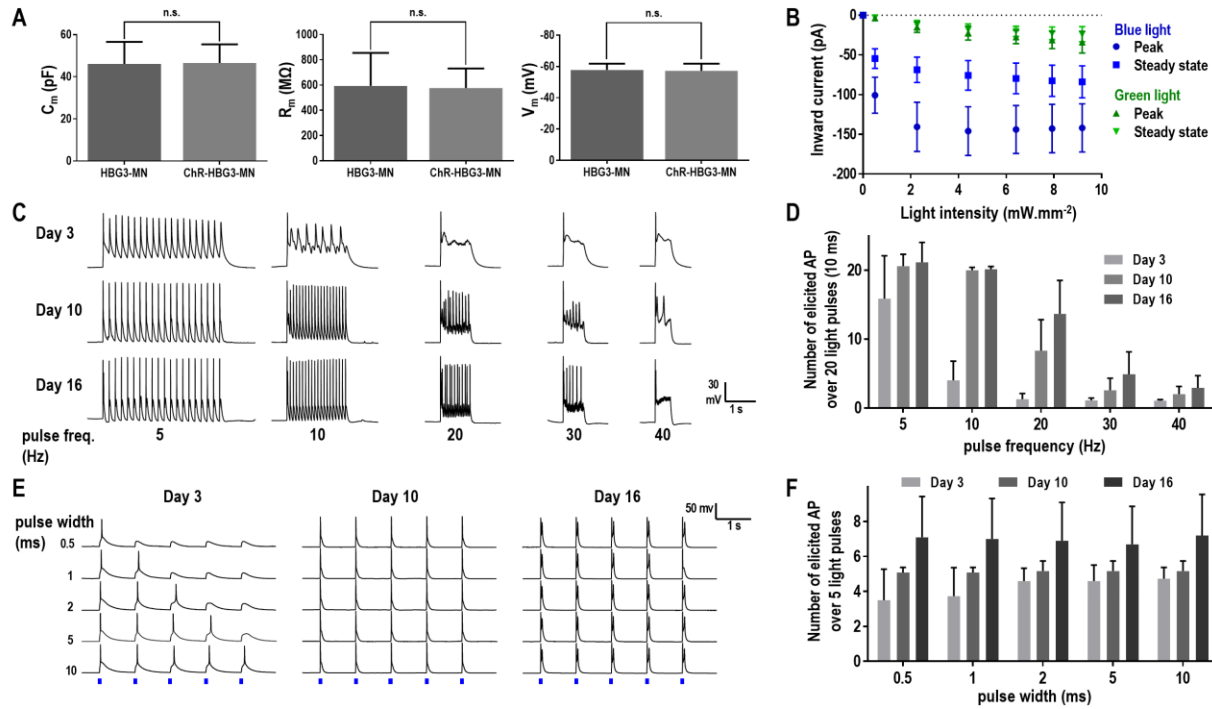


**fig. S2. Electrophysiological characterization of the ChR-HBG3-MN.** (A) Membrane capacitance ( $C_m$ ), membrane resistance ( $R_m$ ) and membrane potential ( $V_m$ ) in motor neurons were not altered by the presence of ChR. (B) Peak and steady state inward current as a function of light intensity for blue and green illumination. (C) Representative action potential elicitation over 20 pulses of light of width 10 ms at frequencies ranging from 5 to 40 Hz, at days 3, 10 and 16. (D) Number of action potentials elicited over 20 pulses of light of increasing frequency. (E) Representative action potential elicitation over 5 pulses of light of width ranging from 0.5 to 10 ms, at days 3, 10 and 16. (F) Number of action potentials elicited over 20 pulses of light of increasing width. All errors bars: STD. n.s. = not significant.



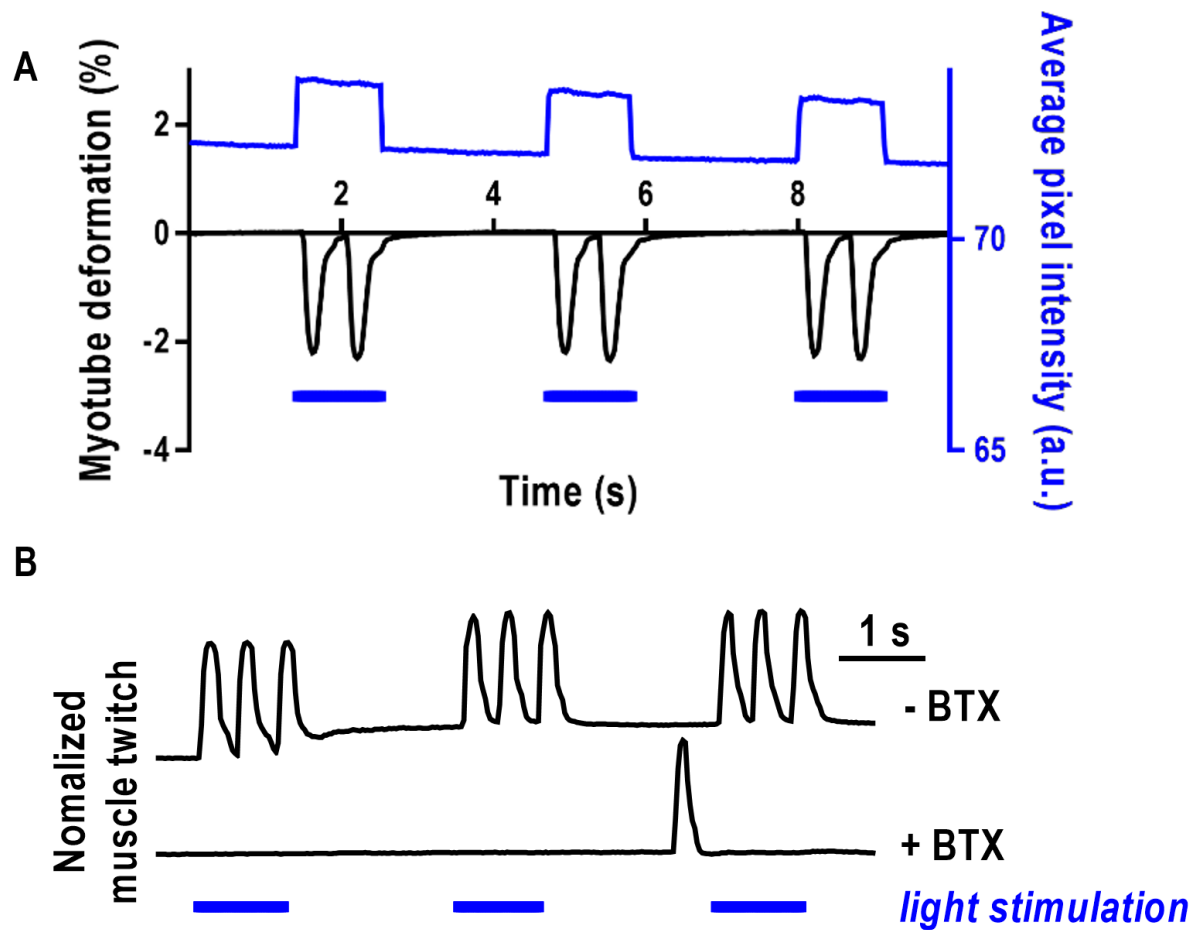


**fig. S3. Optogenetic activation of NMJs in adherent cocultures.** (A) Representative data illustrating the synchronization between the tracking of muscle contraction (black curve, left Y-axis) and the optical stimulation depicted as the average pixel intensity of the gray scale image (blue curve, right Y-axis). The blue bars represent the period of time during which the light is “on”, namely above the resting background pixel intensity. (B) Example of an optogenetic neuronal stimulation of a muscle cell before and after BTX treatment. The presence of a spontaneous twitch indicate that the myofiber was still contractile after BTX application and that the absence of contraction upon illumination is only due to NMJ inhibition.

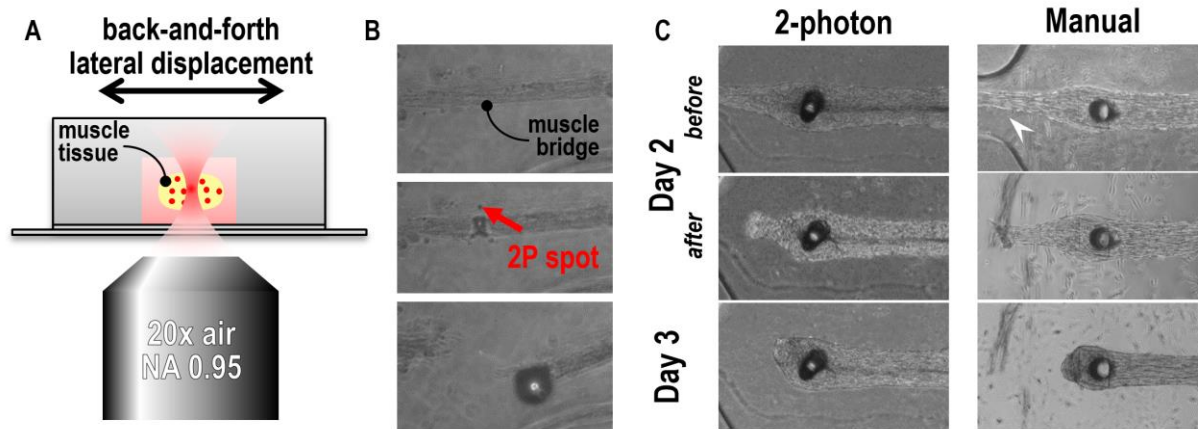


**fig. S4. Modes of tissue ablation.** (A) Schematic depicting the 2P ablation set-up. (B) Thin muscle/hydrogel tissue being dissected by 2P ablation. (C) Comparison of tissue resorption following ablation by 2-photon stimulation or manual dissection.

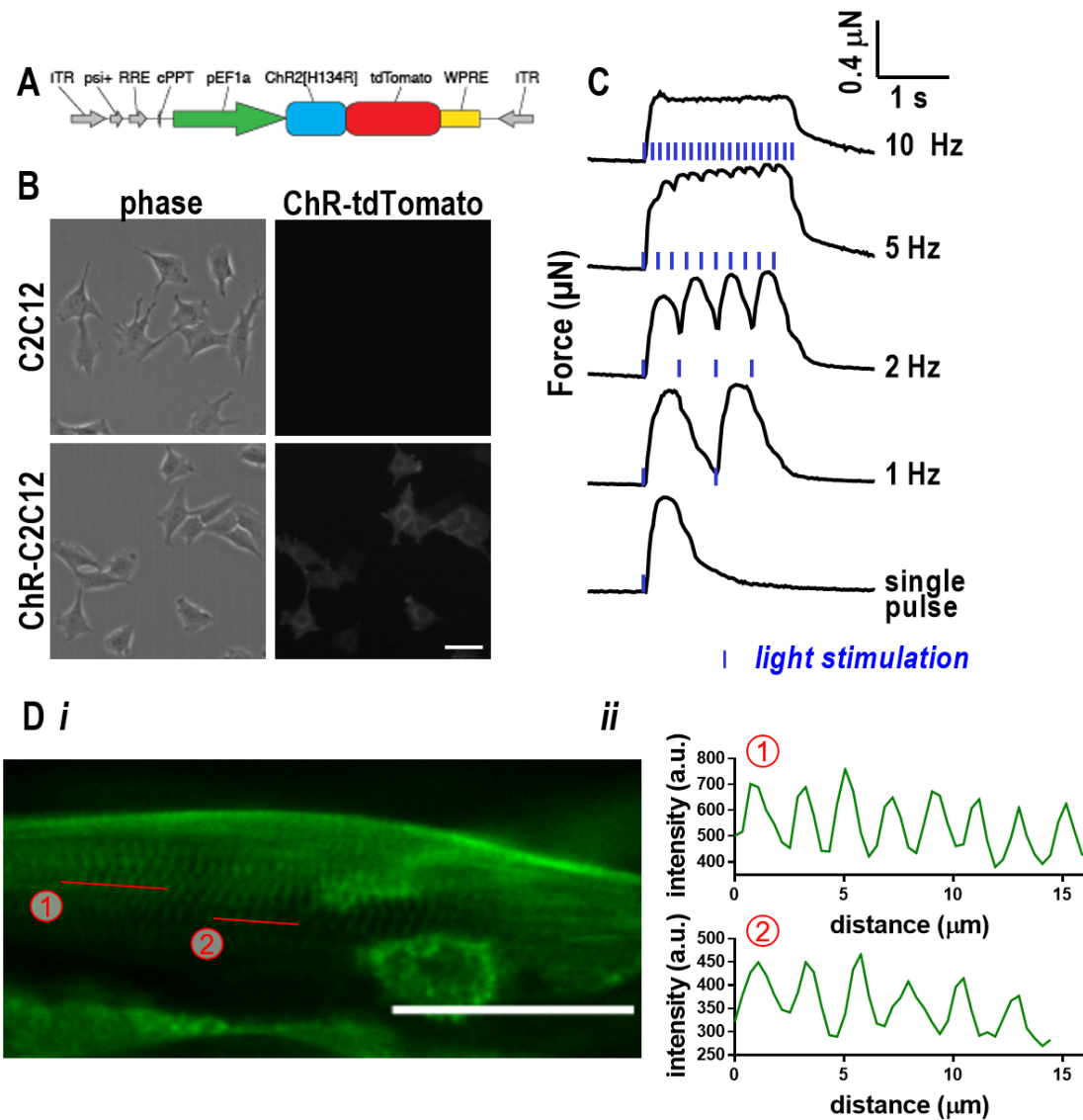


**fig. S5. Photosensitization of the C2C12 myoblasts.** (A) ChR2<sup>H134R</sup> plasmid design for C2C12 viral infection. (B) Comparison of cell morphology and ChR::tdTomato expression between parental C2C12 and ChR2<sup>H134R</sup>-C2C12. Scale bar: 30  $\mu\text{m}$ . (C) Contraction pattern upon light stimulation of muscle bundles derived from ChR2<sup>H134R</sup>-C2C12. (D) (i) Representative image of  $\alpha$ -actinin expression and localization and (ii) quantitative depiction of pixel intensity along the red segments (in (i)), both illustrating the presence of sarcomeric striation.

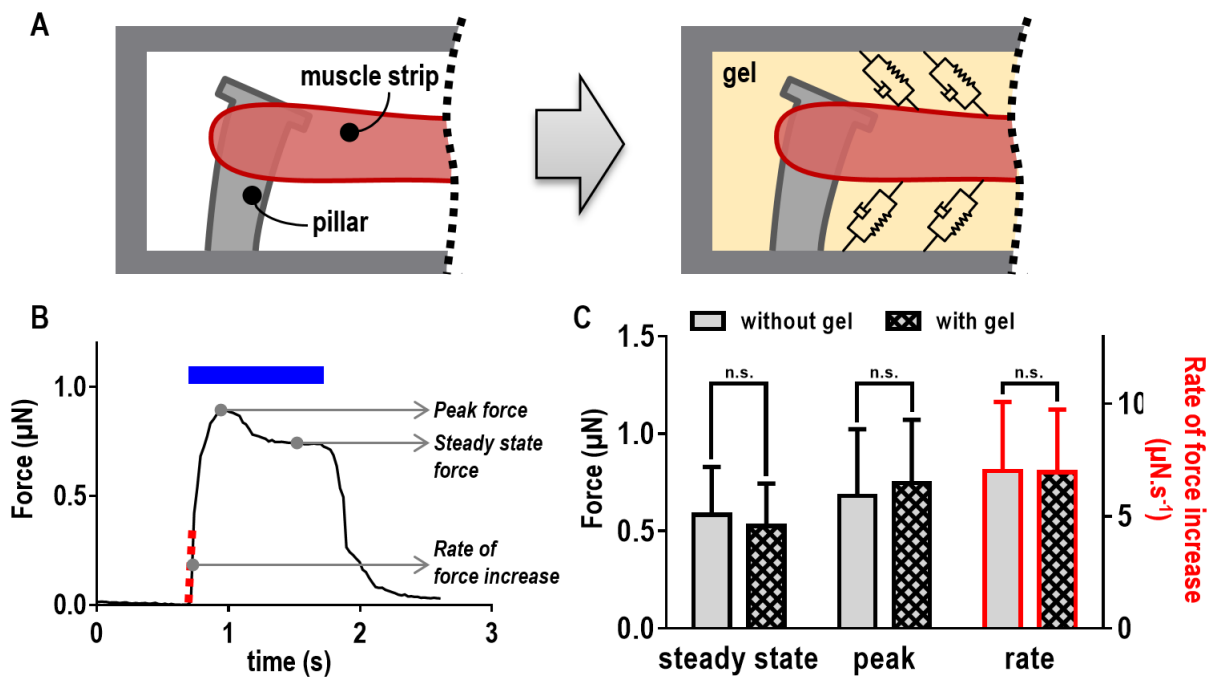


**fig. S6. Influence of the hydrogel on the force measured by the pillar.** (A) Schematic modeling the potential mechanical contributions of a gel surrounding a contractile muscle bundle. (B) Time course of the force generated by the muscle strip upon excitation and measured by the pillar deflection. (C) Comparison of the steady state and peak forces along with the initial rate of force increase before and after the surrounding medium was replaced by the matrix. Error bars: STD. n.s. = not significant.

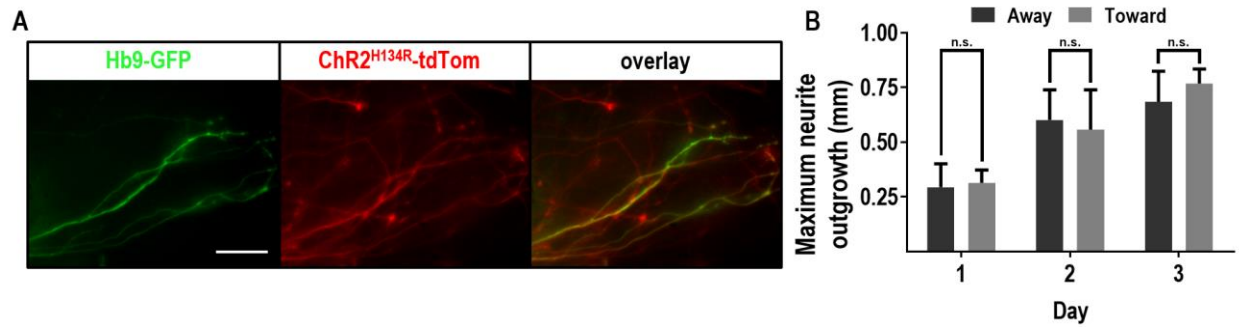


**fig. S7. Motor neurite outgrowth in the microfluidic device:** (A) Epifluorescence images of neurites extending into the extracellular matrix. Scale bar: 50  $\mu$ m. (B) Time course of the maximum neurite outgrowth toward and away from the muscle bundle over the first 3 days of coculture. n.s. = not significant.

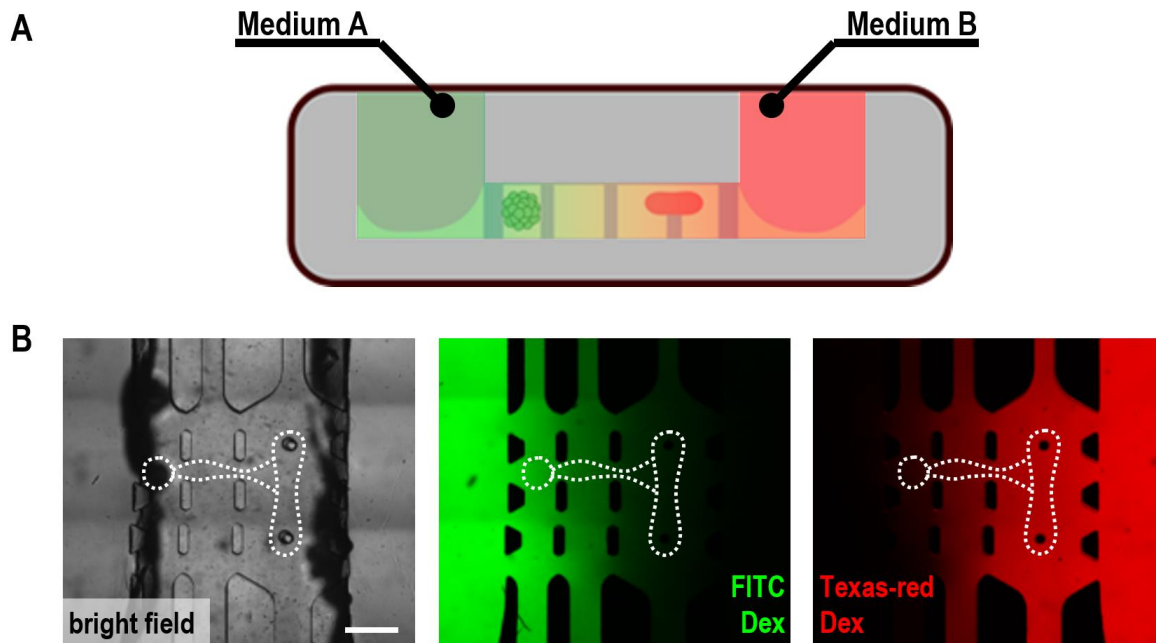


**fig. S8. Opposite gradients as a mean to provide cell specific media. (A)** Schematic illustrating the formation of opposite concentration gradient by supplying each channel with a different medium, a neuron-specific medium A, and a myogenic medium B. **(B)** Fluorescent dextran characterization of the formation of opposite gradients. The white dashed lines materialize where the neurospheres and muscle bundles would be located. Scale bar: 500  $\mu\text{m}$ .

## Supplementary Movie Legends

**movie S1. Muscle contraction upon optical stimulation of ChR-HBG3-MN in adherent cultures.** C2C12-derived myofiber innervated by light activatable motor neurons contracting upon blue light excitation (blue frame and bars). The red dots, indicating the positions of the centers of the regions used for motion tracking, were used to calculate the myotube deformation, as depicted in the graph on the right.

**movie S2. ECM compaction and muscle bundle formation over the first 96 h of the experiment.** C2C12 cells are seeded in the microfluidic device at a density of  $5 \times 10^6$  cells.ml<sup>-1</sup>. The device is placed in an environmental chamber and images are acquired every 30 min. For this experiment, the optogenetically modified ChR2<sup>H134R</sup>-C2C12 cells were used so as to follow each cell via its fluorescence signal. Scale bar: 500  $\mu$ m.

**movie S3. 3D neurite outgrowth in the gel region bridging the neurosphere and the muscle strip.** Confocal reconstruction of the 3D outgrowth of motor neurites (in green) towards the muscle bundle (in red).

**movie S4. Muscle bundle contraction upon light stimulation of the ChR-HBG3-MN in the microfluidic device.** Upon illumination of the photosensitized motor neurons located in the leftmost region of the device (not shown on the movie frame), innervated muscle cells contract, causing deflection of the flexible pillar to which the muscle strip is anchored. Scale bar: 200  $\mu$ m.